Opto-Electronic Advances

Supplementary information

November 2024, Vol. 7, No. 11

DOI: 10.29026/oea.2024.240086

Functionality multiplexing in high-efficiency metasurfaces based on coherent wave interferences

Yuejiao Zhou[1†], Tong Liu[2†], Changhong Dai[1], Dongyi Wang[3*] and Lei Zhou[1,4*]

[1]State Key Laboratory of Surface Physics, Key Laboratory of Micro and Nano Photonic Structures (Ministry of Education), Shanghai Key Laboratory of Metasurfaces for Light Manipulation and Department of Physics, Fudan University, Shanghai 200438, China; [2]Department of Physics, The Hong Kong University of Science and Technology, Clear Water Bay, Kowloon, Hong Kong 999077, China; [3]Department of Physics, Hong Kong Baptist University, Kowloon Tong, Hong Kong 999077, China; [4]Collaborative Innovation Centre of Advanced Microstructures, Nanjing 210093, China.

[†]These authors contributed equally to this work.

*Correspondence: DY Wang, Email: phwang@hkbu.edu.hk; L Zhou, E-mail: phzhou@fudan.edu.cn

This file includes:

Supplementary information for this paper is available at https://doi.org/10.29026/oea.2024.240086

Section 1: Supplementary information for MIM metaatoms

1.1 Simulated phase diagrams for reflectance and reflection phase

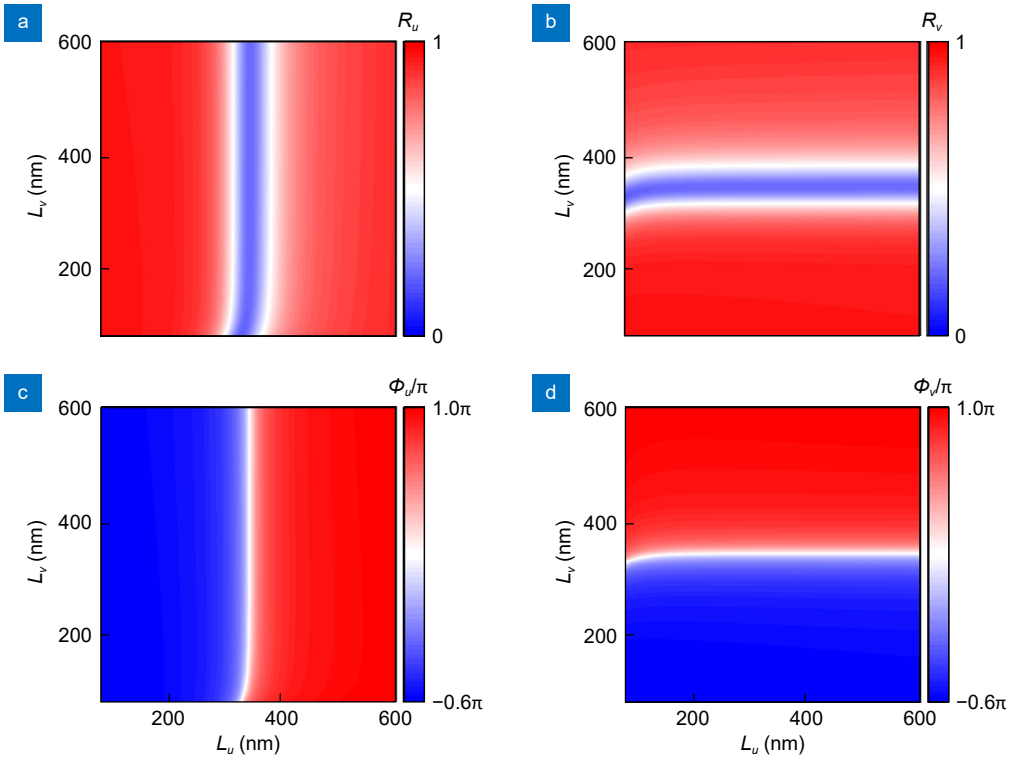

Fig. S1 | FDTD-simulated phase diagrams for reflectance and reflection phase of MIM metaatoms. Reflectance (**a**) $R_u = |r_{uu}|^2$, (**b**) $R_v = |r_{vv}|^2$, and reflection phases (**c**) Φ_u, (**d**) Φ_v for MIM meta-atoms with different L_u and L_v, calculated with FDTD simulations at the working wavelength of 1550 nm. In all our calculations, the metaatoms are repeated along *u* and *v* directions (with periodicity $P_x = P_y = 625$ nm) to form two-dimensional arrays.

1.2 Geometric parameters of 12 metaatoms experimentally characterized in the manuscript

No.	1	2	3	4	5	6	7	8	9	10	11	12
L_u (nm)	285	340	355	410	85	300	330	341	347	355	370	420
L_v (nm)	340	355	425	290	335	355	370	405	220	300	330	340

1.3 SEM images of 12 metaatoms experimentally characterized in the manuscript

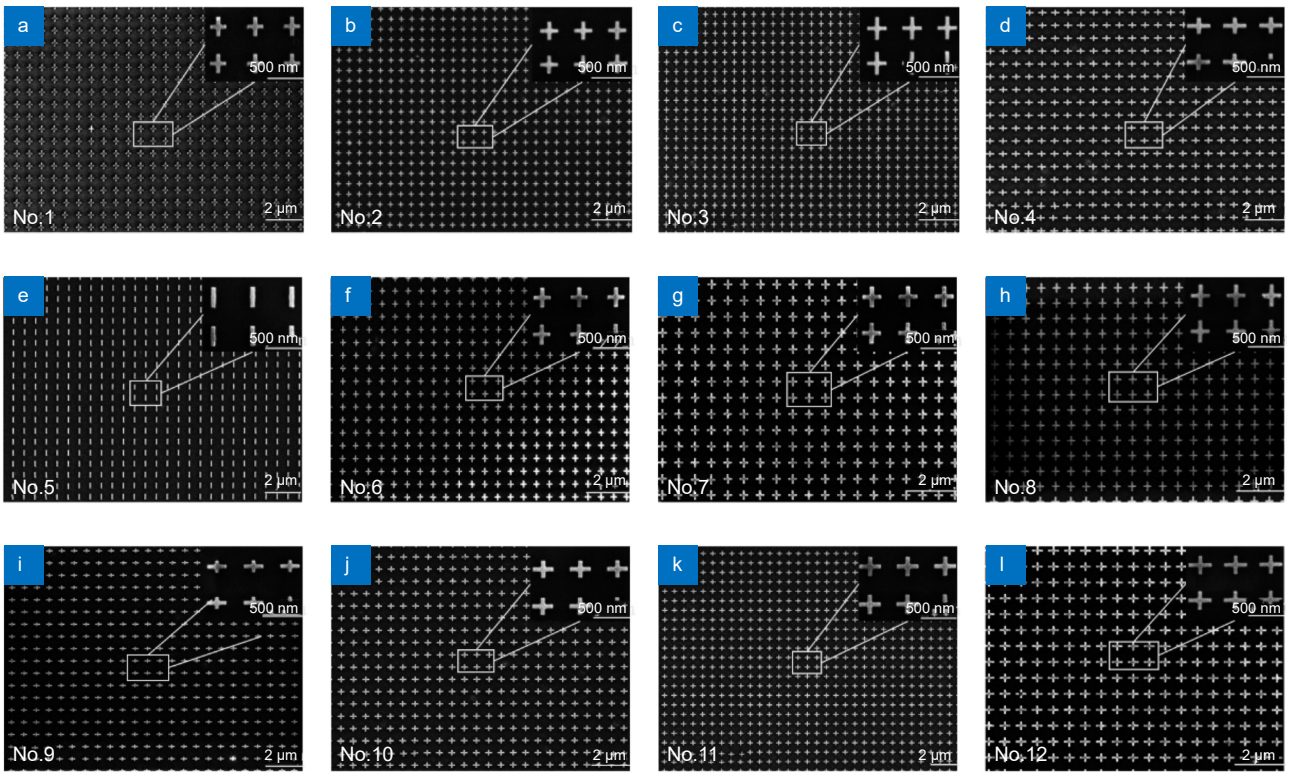

Fig. S2 | SEM images of 12 metaatoms demonstrated in the manuscript.

1.4 FDTD-calculated phase responses of 12 metaatoms experimentally characterized in the manuscript

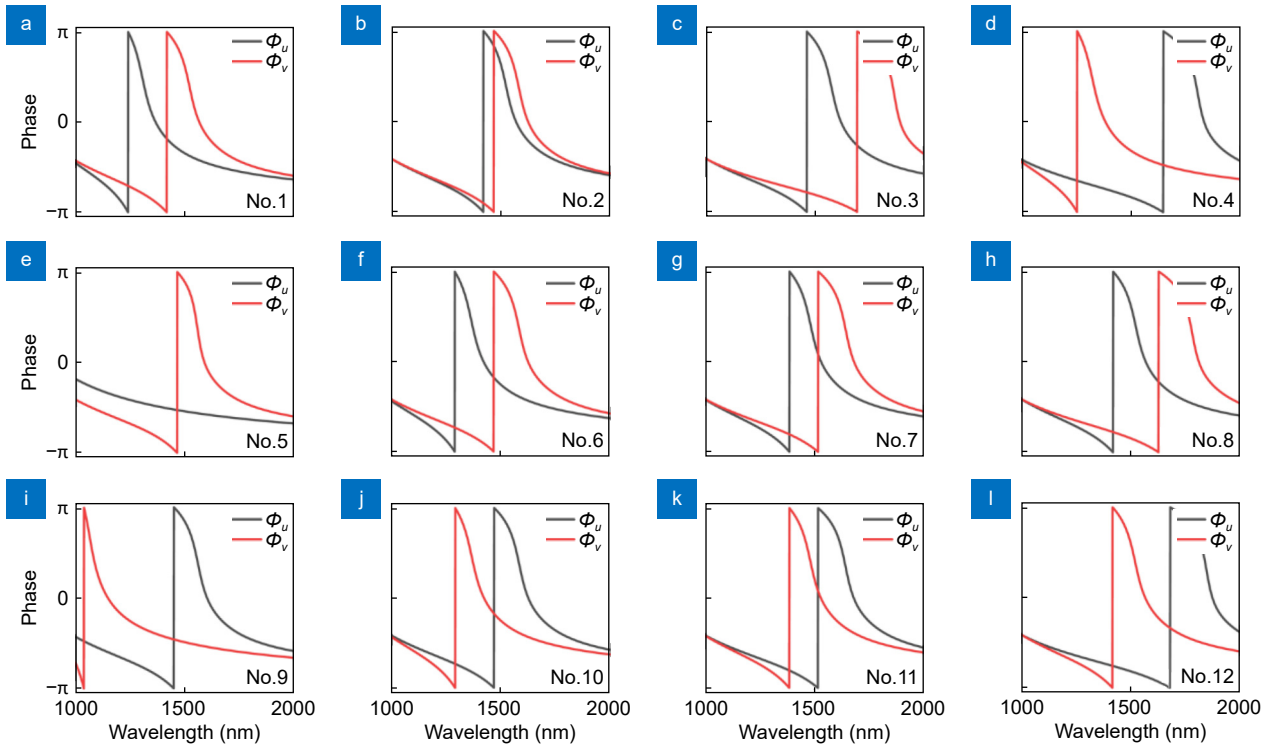

Fig. S3 | FDTD-calculated reflection-phase spectra for 12 metaatoms experimentally characterized in the manuscript. In all our calculations, the metaatoms are repeated along *u* and *v* directions (with periodicity $P_x = P_y = 625$ nm) to form two-dimensional arrays.

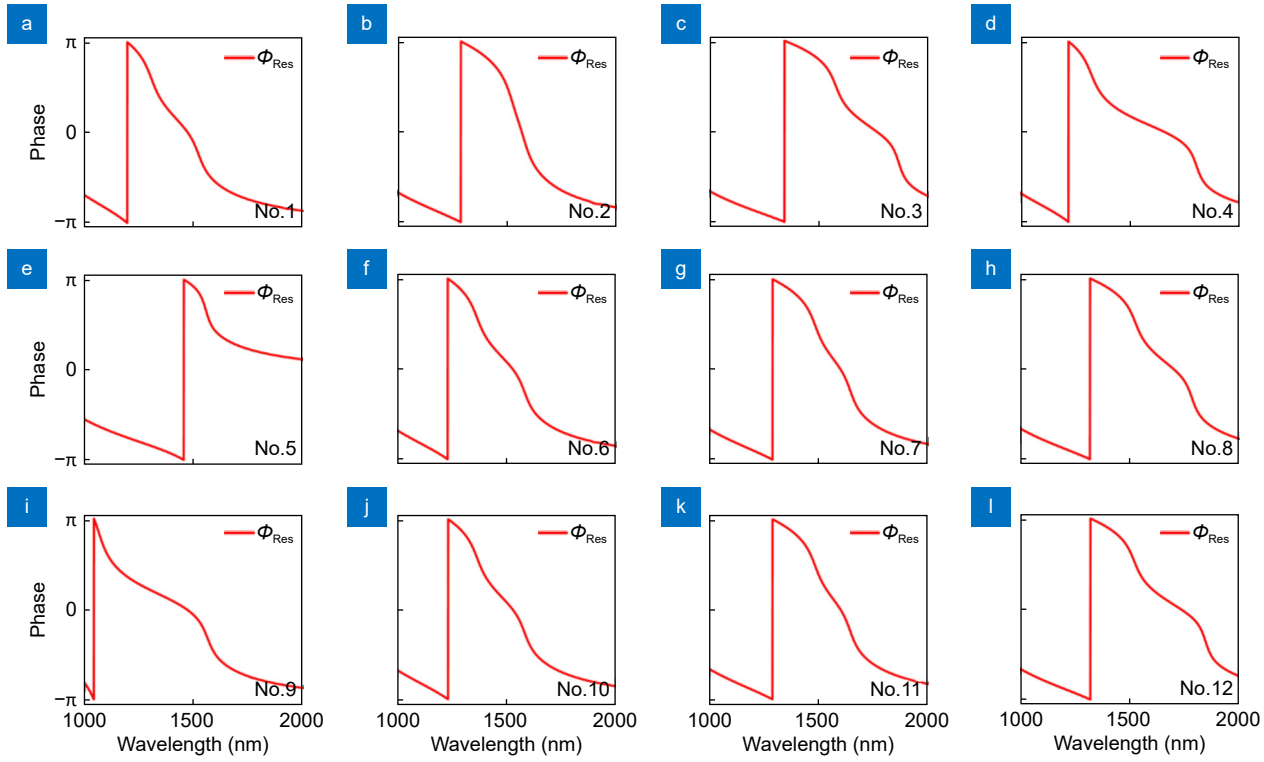

Fig. S4 | FDTD-calculated spectra of resonant phases for 12 metaatoms experimentally characterized in the manuscript. The resonant phase is defined by $\Phi_{Res} = (\Phi_u + \Phi_v)/2 - \pi/4$.

1.5 Polarizer-filtered intensity patterns of 12 metaatoms

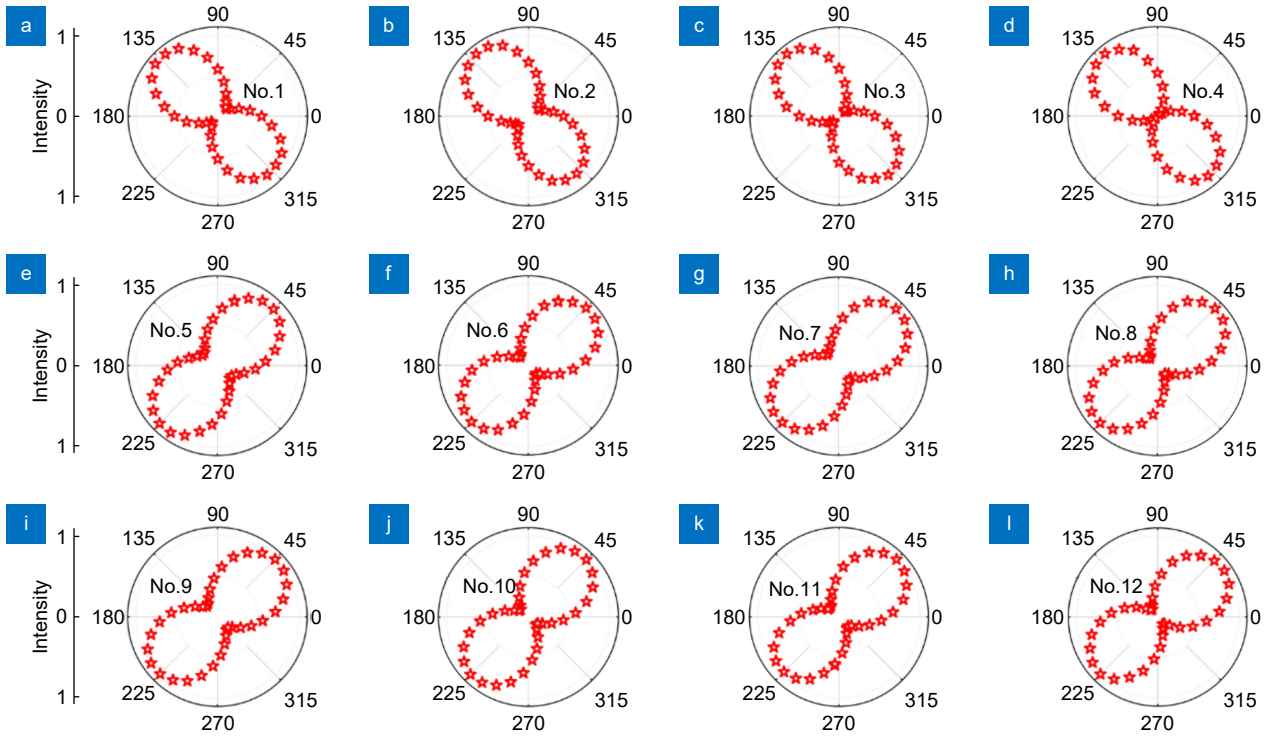

Fig. S5 | Measured polarizer-filtered intensity patterns for light waves reflected by 12 metaatoms experimentally characterized in the manuscript. The polarization of incident light is LCP for (**a**–**d**) and is LP with *E* field polarized along the angle 135° for (**e**–**l**). In all cases, the metaatoms are repeated along *u* and *v* directions (with periodicity $P_x = P_y = 625$ nm) to form two-dimensional arrays, and the working wavelength is 1550 nm.

1.6 Simulated reflection phase diagrams

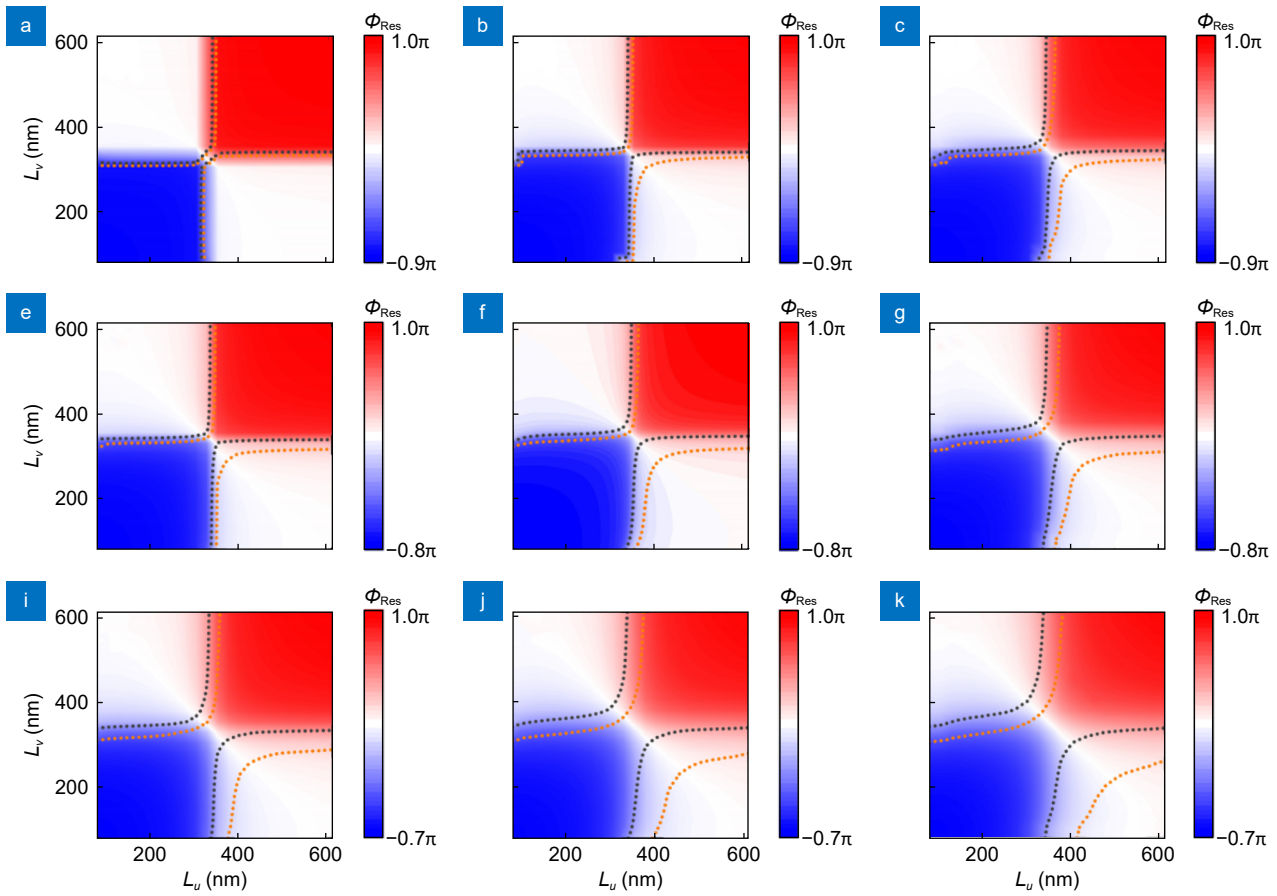

Fig. S6 | FDTD-simulated reflection phase diagrams of MIM metaatoms. Resonant phase Φ_{Res} of metaatoms with different spacer thicknesses d_{int} and bar widths w when varying L_u and L_v at the wavelength of 1550 nm. (a) d_{int} = 100 nm, w = 60 nm; (b) d_{int} = 100 nm, w = 80 nm; (c) d_{int} = 100 nm, w = 100 nm; (d) d_{int} = 120 nm, w = 60 nm; (e) d_{int} = 120 nm, w = 80 nm; (f) d_{int} = 120 nm, w = 100 nm; (g) d_{int} = 140 nm, w = 60 nm; (h) d_{int} = 140 nm, w = 80 nm; (i) d_{int} = 140 nm, w = 100 nm. Orange dashed lines denote the cases $\Delta\Phi$ = 0.5π and −1.5π and black dashed lines denote the cases $\Delta\Phi$ = ±π. The thickness of SiO_2 spacer and widths of metallic bars are selected and fixed to be d_{int} = 120 nm, w = 80 nm to obtain larger resonant phase coverage and not-too-abrupt phase change when varying L_u and L_v for the convenience of metadevice design.

Section 2: Theoretical analyses on the proposed metadevices

2.1 Theoretical analyses on interference patterns

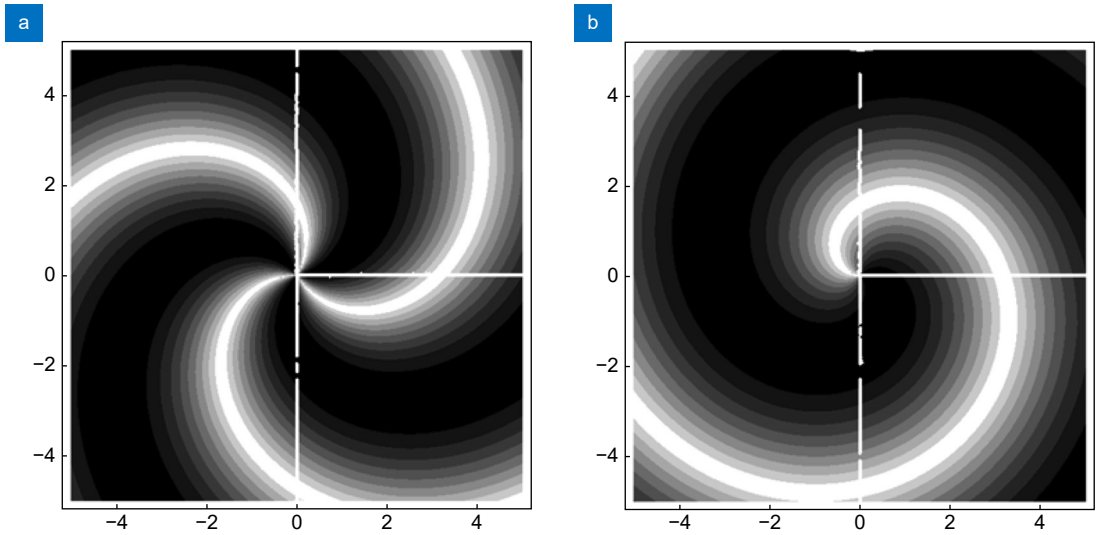

Fig. S7 | Theoretically calculated interference patterns of metadevice I. Theoretically calculated interference patterns between a spherical wave and the (**a**) LCP component and (**b**) RCP component of the waves reflected by meta-device I.

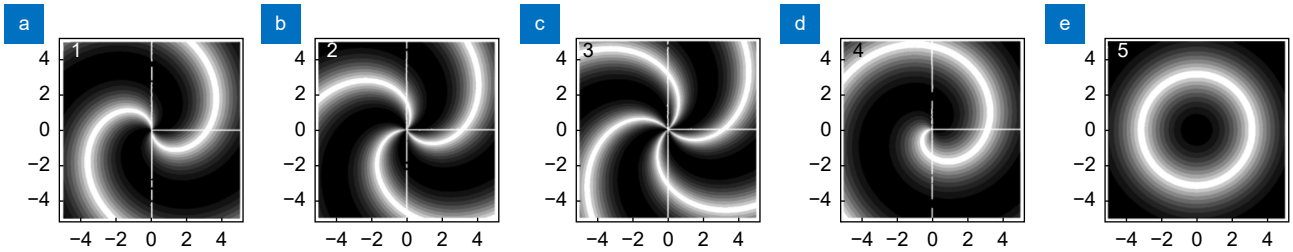

Fig. S8 | Theoretically calculated interference patterns of Meta-device II. Theoretically calculated interference patterns between a spherical wave and the waves reflected by the metasurface, as shined by normally incident light at 1550 nm with polarizations corresponding to points (**a**) 1, (**b**) 2, (**c**) 3, (**d**) 4, and (**e**) 5 on Poincare' sphere as shown in Fig. 4(b) in the manuscript.

2.2 Derivation of Eqs. (2,3) in the manuscript

We first neglect material losses as we establish the theoretical framework, i.e. suppose that $|r_{uu}| = |r_{vv}| = 1$, $r_{uu} = \mathrm{e}^{\mathrm{i}\Phi_u}$ and $r_{vv} = \mathrm{e}^{\mathrm{i}\Phi_v}$. Later we find from the experimental results that adding losses back does not significantly change the established framework. As mentioned in the main text, the Jones-Matrix in CP bases is

$$\tilde{\boldsymbol{R}} = \boldsymbol{S}\boldsymbol{M}(\xi)\begin{pmatrix} r_{uu} & 0 \\ 0 & r_{vv} \end{pmatrix}\boldsymbol{M}(\xi)^{-1}\boldsymbol{S}^{-1} = \mathrm{e}^{\mathrm{i}\frac{\Phi_u+\Phi_v}{2}}\begin{pmatrix} \cos\dfrac{\Phi_v-\Phi_u}{2} & \mathrm{e}^{-\mathrm{i}(2\xi+\frac{\pi}{2})}\sin\dfrac{\Phi_v-\Phi_u}{2} \\ \mathrm{e}^{+\mathrm{i}(2\xi-\frac{\pi}{2})}\sin\dfrac{\Phi_v-\Phi_u}{2} & \cos\dfrac{\Phi_v-\Phi_u}{2} \end{pmatrix}. \tag{S1}$$

Under LCP illumination, the scattered waves can be written as:

$$\tilde{\boldsymbol{R}}|+\rangle = \begin{pmatrix} \cos\dfrac{\Phi_v-\Phi_u}{2} \\ \mathrm{e}^{+\mathrm{i}(2\xi-\frac{\pi}{2})}\sin\dfrac{\Phi_v-\Phi_u}{2} \end{pmatrix} = \mathrm{e}^{\mathrm{i}\Phi^+}\begin{pmatrix} \mathrm{e}^{-\mathrm{i}\Psi^+/2}\cos(\Theta^+/2) \\ \mathrm{e}^{\mathrm{i}\Psi^+/2}\sin(\Theta^+/2) \end{pmatrix}, \tag{S2}$$

where

$$\begin{cases} \Phi^{+} = \dfrac{\Phi_u + \Phi_v}{2} - \dfrac{\pi}{4} + \xi \\ \Theta^{+} = \Phi_v - \Phi_u \\ \Psi^{+} = 2\xi - \dfrac{\pi}{2} \end{cases} . \tag{S3}$$

While under RCP illumination, the scattered waves can be written as:

$$\tilde{\boldsymbol{R}}\left|-\right\rangle = \mathrm{e}^{\mathrm{i}\frac{\Phi_u+\Phi_v}{2}} \begin{pmatrix} \mathrm{e}^{-\mathrm{i}(2\xi+\frac{\pi}{2})}\sin\dfrac{\Phi_v-\Phi_u}{2} \\ \cos\dfrac{\Phi_v-\Phi_u}{2} \end{pmatrix} = \mathrm{e}^{\mathrm{i}\Phi^{-}} \begin{pmatrix} \mathrm{e}^{-\mathrm{i}\Psi^{-}/2}\cos(\Theta^{-}/2) \\ \mathrm{e}^{\mathrm{i}\Psi^{-}/2}\sin(\Theta^{-}/2) \end{pmatrix} , \tag{S4}$$

where

$$\begin{cases} \Phi^{-} = \dfrac{\Phi_u + \Phi_v}{2} - \dfrac{\pi}{4} - \xi \\ \Theta^{-} = \pi - (\Phi_v - \Phi_u) \\ \Psi^{-} = 2\xi + \dfrac{\pi}{2} \end{cases} . \tag{S5}$$

Thus, for the incident CP components possessing different helicities ($\sigma = \pm 1$), we have

$$\tilde{\boldsymbol{R}}\left|\sigma\right\rangle = \mathrm{e}^{\mathrm{i}\Phi^{\sigma}} \begin{pmatrix} \mathrm{e}^{-\mathrm{i}\Psi^{\sigma}/2}\cos(\Theta^{\sigma}/2) \\ \mathrm{e}^{\mathrm{i}\Psi^{\sigma}/2}\sin(\Theta^{\sigma}/2) \end{pmatrix} , \tag{S6}$$

where

$$\begin{cases} \Phi^{\sigma} = \Phi_{\mathrm{Res}} + \Phi_{\mathrm{PB}} \\ \Theta^{\sigma} = \sigma\left(\Delta\Phi - \dfrac{\pi}{2}\right) + \dfrac{\pi}{2} \\ \Psi^{\sigma} = 2\xi - \sigma\dfrac{\pi}{2} \end{cases} , \tag{S7}$$

with $\Phi_{\mathrm{Res}} = (\Phi_u + \Phi_v)/2 - \pi/4$ and $\Phi_{\mathrm{PB}} = \sigma \cdot \xi$. Thus we obtain Eqs. (S6, S7) which are exactly the same as Eqs (2, 3) in the main text.

2.3 Derivation of Eqs. (6,7) in the manuscript

As mentioned in the main text, metadevice II is requested to exhibit spin-dependent distributions of reflection phase and polarization state defined by Eq. (5). Combining Eq. (2) we have

$$\tilde{\boldsymbol{R}}\left|+\right\rangle = \mathrm{e}^{\mathrm{i}4\phi} \begin{pmatrix} 0 \\ 1 \end{pmatrix} , \tag{S8}$$

and

$$\tilde{\boldsymbol{R}}\left|-\right\rangle = \begin{pmatrix} 1 \\ 0 \end{pmatrix} . \tag{S9}$$

Suppose that the incident polarization is an EP one with $\left|\boldsymbol{\sigma}_0\right\rangle = A_+\left|+\right\rangle + A_-\left|-\right\rangle$, the reflected wave can be mapped to a general form

$$\tilde{\boldsymbol{R}}\left|\widehat{\sigma}_0\right\rangle = A_+\tilde{\boldsymbol{R}}\left|+\right\rangle + A_-\tilde{\boldsymbol{R}}\left|-\right\rangle = \begin{pmatrix} A_- \\ A_+\mathrm{e}^{\mathrm{i}4\phi} \end{pmatrix} \equiv \mathrm{e}^{\mathrm{i}\Phi_{\mathrm{tar}}^{\mathrm{EP}}(\vec{r})} \begin{pmatrix} \mathrm{e}^{-\mathrm{i}\Psi_{\mathrm{tar}}^{\mathrm{EP}}(\boldsymbol{r})/2}\cos(\Theta_{\mathrm{tar}}^{\mathrm{EP}}(\boldsymbol{r})/2) \\ \mathrm{e}^{+\mathrm{i}\Psi_{\mathrm{tar}}^{\mathrm{EP}}(\boldsymbol{r})/2}\sin(\Theta_{\mathrm{tar}}^{\mathrm{EP}}(\boldsymbol{r})/2) \end{pmatrix} . \tag{S10}$$

For the general case where $|A_+| \cdot |A_-| \neq 0$, we have

$$\begin{cases} \Phi_{\mathrm{tar}}^{\mathrm{EP}}(\boldsymbol{r}) = 2\phi + \dfrac{\arg(A_+) + \arg(A_-)}{2} \\ \Theta_{\mathrm{tar}}^{\mathrm{EP}}(\boldsymbol{r}) = 2\arctan\dfrac{|A_+|}{|A_-|} \\ \Psi_{\mathrm{tar}}^{\mathrm{EP}}(\boldsymbol{r}) = 4\phi + \arg(A_+) - \arg(A_-) \end{cases} , \tag{S11}$$

thus we obtain Eq (S11), which is exactly the same as Eq. (6) in the main text.

Mathematically consider a vectorial field propagating along z direction generated by the metasurface at the incidence of a general EP light, denoted by $\boldsymbol{E}(\boldsymbol{r}) = \left[\mathrm{e}^{-\mathrm{i}\Psi_{\mathrm{tar}}^{\mathrm{EP}}(r)/2}\cos\left(\Theta_{\mathrm{tar}}^{\mathrm{EP}}(\boldsymbol{r})/2\right)\hat{e}_{+} + \mathrm{e}^{\mathrm{i}\Psi_{\mathrm{tar}}^{\mathrm{EP}}(r)/2}\sin\left(\Theta_{\mathrm{tar}}^{\mathrm{EP}}(\boldsymbol{r})/2\right)\hat{e}_{-}\right] \mathrm{e}^{\mathrm{i}\Phi_{\mathrm{tar}}^{\mathrm{EP}}(r)} + E_z(\boldsymbol{r})\hat{z} = \left[\frac{1}{\sqrt{2}}\left(\mathrm{e}^{-\mathrm{i}\Psi_{\mathrm{tar}}^{\mathrm{EP}}(r)/2}\cos\left(\Theta_{\mathrm{tar}}^{\mathrm{EP}}(\boldsymbol{r})/2\right) + \mathrm{e}^{\mathrm{i}\Psi_{\mathrm{tar}}^{\mathrm{EP}}(r)/2}\sin\left(\Theta_{\mathrm{tar}}^{\mathrm{EP}}(\boldsymbol{r})/2\right)\right)\hat{x} + \frac{\mathrm{i}}{\sqrt{2}}\left(\mathrm{e}^{-\mathrm{i}\Psi_{\mathrm{tar}}^{\mathrm{EP}}(r)/2}\cos\left(\Theta_{\mathrm{tar}}^{\mathrm{EP}}(\boldsymbol{r})/2\right) - \mathrm{e}^{\mathrm{i}\Psi_{\mathrm{tar}}^{\mathrm{EP}}(r)/2}\sin\left(\Theta_{\mathrm{tar}}^{\mathrm{EP}}(\boldsymbol{r})/2\right)\right)\hat{y}\right] \mathrm{e}^{\mathrm{i}\Phi_{\mathrm{tar}}^{\mathrm{EP}}(r)} + E_z(\boldsymbol{r})\hat{z}$. Under paraxial approximation, the time-average energy per unit length along z direction is

$$U = \int \langle e\rangle \,\mathrm{d}^2\boldsymbol{r}_{\perp} = \frac{1}{2}\int \left\langle \varepsilon_0|E|^2 + \frac{|B|^2}{\mu_0}\right\rangle \mathrm{d}^2\boldsymbol{r}_{\perp} = \frac{\varepsilon_0}{2}\mathrm{Re}\left[\int \left(E_x^* E_x + E_y^* E_y\right)\mathrm{d}^2\boldsymbol{r}_{\perp}\right] = \frac{\varepsilon_0}{2}\int \mathrm{d}^2\boldsymbol{r}_{\perp}\,, \tag{S12}$$

and the time-average OAM per unit length along z direction is:

$$\begin{aligned}\Lambda_z &= \int \left\langle l_z\left(\overrightarrow{r}\right)\right\rangle \mathrm{d}^2\boldsymbol{r}_{\perp} = \frac{\varepsilon_0}{2\omega}\int \mathrm{Im}\left[\sum_{m=x,y} E_m^*(\boldsymbol{r}\times\nabla)_z E_m\right]\mathrm{d}^2\boldsymbol{r}_{\perp} \\ &= \frac{\varepsilon_0}{2\omega}\int \sum_{m=x,y}|E_m|^2\frac{\partial \arg\left(E_m\right)}{\partial\phi}\mathrm{d}^2\boldsymbol{r}_{\perp} = \frac{\varepsilon_0}{2\omega}\int\left[\frac{\partial\Phi_{\mathrm{tar}}^{\mathrm{EP}}}{\partial\phi} - \frac{1}{2}\cos\Theta_{\mathrm{tar}}^{\mathrm{EP}}\frac{\partial\Psi_{\mathrm{tar}}^{\mathrm{EP}}}{\partial\phi}\right]\mathrm{d}^2\boldsymbol{r}_{\perp}\,.\end{aligned} \tag{S13}$$

Together with Eq. (6) in the manuscript, we then can derive expression for averaged OAM per photon carried by the light beam, which is just Eq. (7) in the main text.

$$L_z = \hbar\omega\frac{\Lambda_z}{U} = \left[2 - 2\cos\left(2\arctan\frac{|A_+|}{|A_-|}\right)\right]\hbar\,, \tag{S14}$$

Section 3: Experimental setups

3.1 Experimental set-up for characterizations of metaatoms Nos. 1–12

The experimental setup employed for characterization of metaatoms is schematically shown in Fig. S9. The optical path consists of two parts: the incident path and the imaging path. In the incident path, the intensity of light is tuned by an attenuator, and the polarization is tuned by relative angle between the linear polarizer (LP) and the quarter-wave-plate (QWP). The incident light is focused onto the sample and subsequently reflected, and then directed into the imaging path by a BS and a mirror, and finally focused by a lens and collected by the NIR spectrometer in the imaging path.

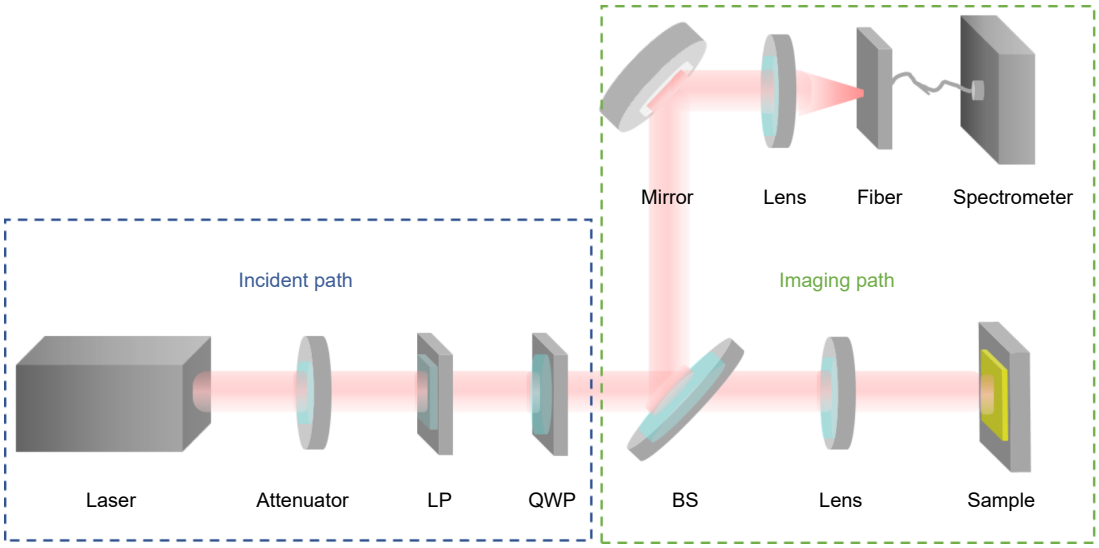

Fig. S9 | Schematics of the experimental setup for characterizations of metaatoms Nos. 1–12. Here, LP represents linear Polarizer, QWP represents quarter wave plate, and BS represents beam splitting lens.

3.2 Experimental setup for characterizations of metadevice I

A home-made macro-angular-resolution spectroscopy is employed for characterizating metadevice I, as schematically depicted in Fig. S10. The optical path consists of three parts: the incident path, the imaging path, and the interference path. The intensity of incident light is tuned by an attenuator, and the polarization is tuned by varying the relative angle δ between the LP and the QWP. On the imaging path, the sample can be tilted at different angles by the RS1, while the CCD/optical fibre connected to a spectrometer for data collection can be correspondingly tilted by the RS2. Thus, light reflected to different angles can be collected by rotating RS2. The interference path consists of BS, a lens and a mirror placed at suitable positions. The combination of QWP and LP is employed for polarization control of the interference light.

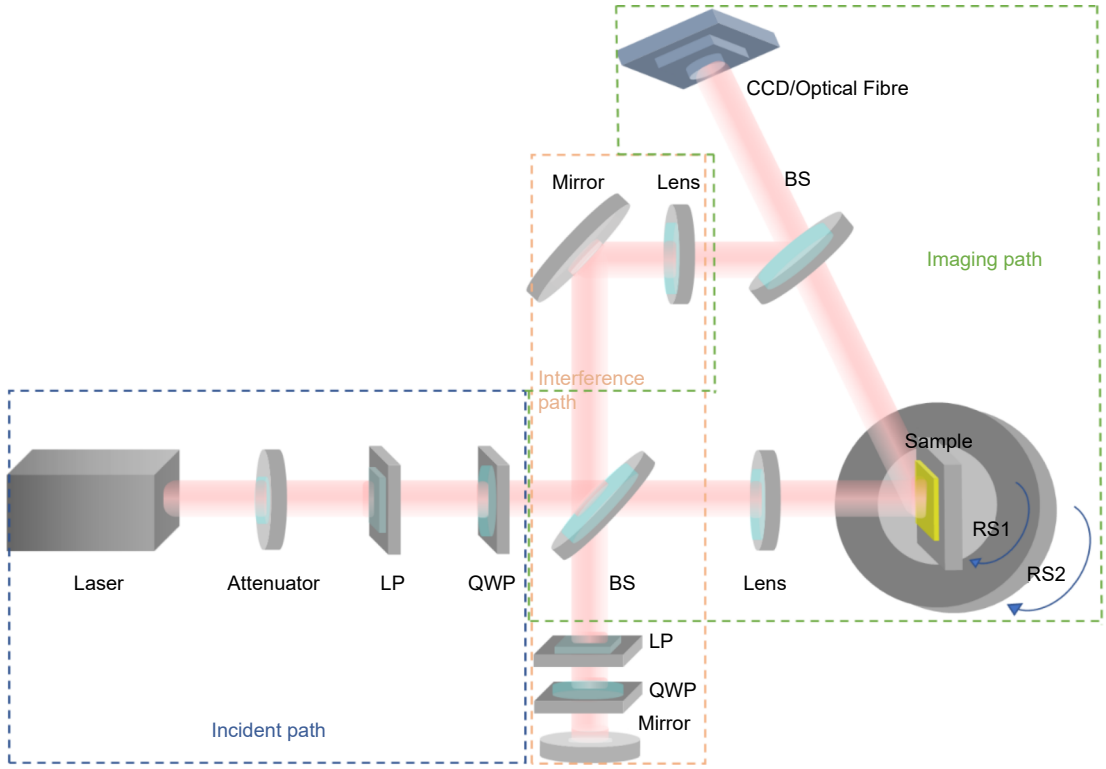

Fig. S10 | Schematics of the macro-angular-resolution spectroscopy for characterizations of metadevice I. Here, RS represents the rotatable stage.

3.3 Experimental setup for characterizations of metadevice II and experimental analyses on $\{\gamma_0, \varphi_0\}$

A home-made Michelson interferometer is employed for characterizing metadevice II, as schematically depicted in Fig. S11. The optical path consists of three parts: the incident path, the imaging path, and the interference path. The intensity of incident light is tuned by an attenuator, and the polarization is tuned by varying the angle δ. On the imaging path, the incident light is reflected by the sample and is collected by the NIR CCD. A rotatable LP is placed in front of the CCD for characterizing LPD property of the reflected light beam. The interference path consists of a BS, a lens and a mirror placed at suitable positions. The combination of QWP and LP is employed for polarization control of the interference light.

Based on the CCD-captured results shown in Fig. 4(f–j) and Fig. 5(e–h), $\{\gamma_0, \varphi_0\}$ can be easily retrieved. In each figure, when the polarizer for LPD analysis is tilted at 0°, the polar-angle positions with the minimum and maximum measured intensities can identified as $\phi_{\max}$, $\phi_{\min}$, and φ_0 is directly obtained as

$$\varphi_0 = \frac{\pi}{2} + n\pi - 2\phi_{\min} , \tag{S15}$$

where $n \in Z$ is an arbitrarily selected integer to satisfy the condition of $\varphi_0 \in \left[-\frac{\pi}{2}, \frac{\pi}{2}\right]$. The line-integrals along the

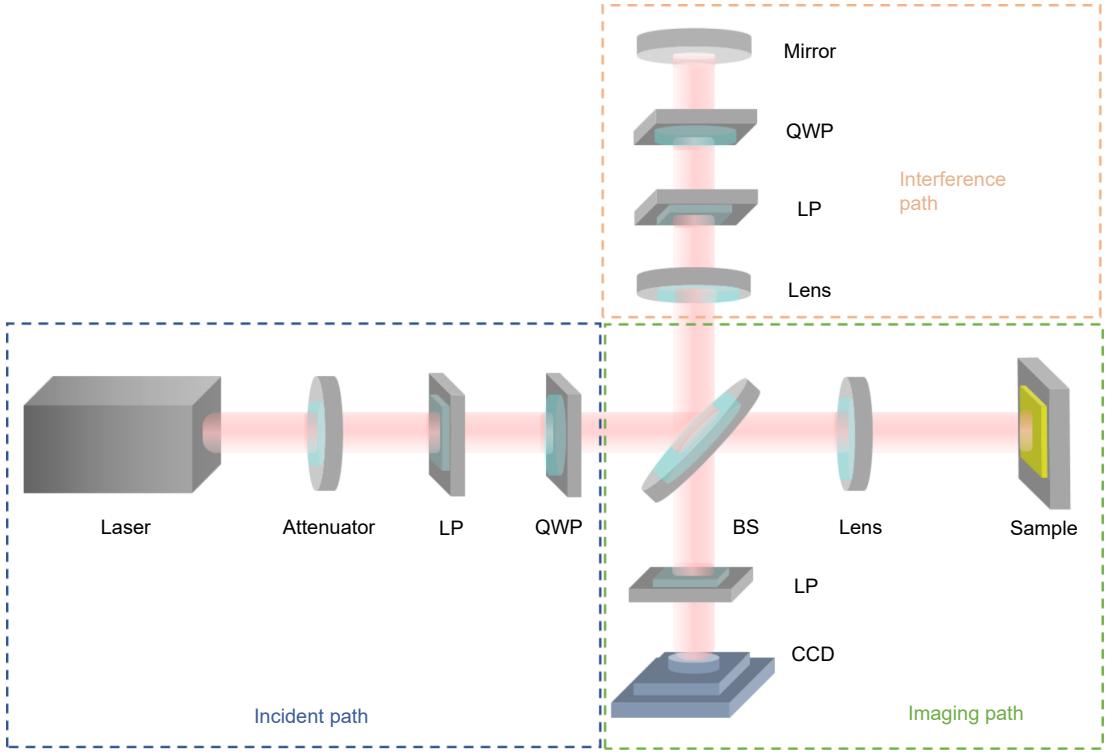

Fig. S11 | Schematics of the Michelson interferometer for characterizations of metadevice II.

radial direction at the corresponding polar angle with the minimum and maximum measured intensities denote $I_{\max} = \int_{r,\phi=\phi_{\max}} I_r$ and $I_{\min} = \int_{r,\phi=\phi_{\min}} I_r$ respectively, thus the experimentally measured ellipticity can be obtained by

$$\gamma_0 = -\sigma_0 \left(1 - \frac{|I_{\max} - I_{\min}|}{I_{\max} + I_{\min}}\right) , \tag{S16}$$

with $\sigma_0 = +1$ if the incident polarization lies on the upper Poincare's sphere and $\sigma_0 = -1$ vice versa.

Section 4: Evaluation on working efficiencies

Taking material losses of the meta-atoms into consideration, we capture the optical properties of meta-atoms at a specific position $\boldsymbol{r}$ with complex reflection coefficients $r_{uu}(\boldsymbol{r})$, $r_{vv}(\boldsymbol{r})$ where $|r_{uu}(\boldsymbol{r})|$, $|r_{vv}(\boldsymbol{r})| < 1$, obtained from full-wave simulations. The reflected beam is thus denoted by:

$$\tilde{\boldsymbol{R}}|\sigma\rangle = A_n e^{i\arg(r_{uu}+r_{vv})}|\sigma\rangle + A_a e^{i[\arg(r_{uu}-r_{vv})+\sigma\cdot 2\xi]}|-\sigma\rangle , \tag{S17}$$

with $A_n = \left|\frac{r_{uu}+r_{vv}}{2}\right|$, $A_a = \left|\frac{r_{uu}-r_{vv}}{2}\right|$ being intensity ratios of normal and abnormal modes in the reflected wave, A_a denoting the desired component, thus the working efficiency of an individual meta-atom can be expressed by:

$$\eta = |A_a|^2 . \tag{S18}$$

We then evaluate the working efficiencies of the two meta-devices by calculating the efficiencies of each and every constituent meta-atom then taking the average value. With such strategy, the average efficiencies of meta-device I, II are assessed to be $\bar{\eta}_{\mathrm{I}} = 28.2\%$ and $\bar{\eta}_{\mathrm{II}} = 28.9\%$, respectively.